

A MATHEMATICAL MODEL AND NUMERICAL SOLUTION TECHNIQUE FOR A NOVEL ADJUSTABLE HYDRODYNAMIC BEARING

J.K. MARTIN*

Engineering Mechanics Lubrication Research Group, The Open University, Milton Keynes, MK14 5AS, UK

SUMMARY

An analysis model for a novel adjustable hydrodynamic fluid film bearing is described. The principles of hydrodynamic lubrication are outlined together with an expanded version of the governing pressure field equation as related to the novel bearing. Finite difference approximations are given for the pressure field equation and a temperature model, both related to the fluid film thickness. Relationships of viscosity with temperature and pressure are included. A finite element model and an iterative computational process are described, whereby full simultaneously converged field solutions for fluid film thickness, temperature, viscosity and pressure were obtained, together with oil film forces. The model and solution process were developed to apply to a variety of hydrodynamic bearings and an outline is given of its extensive use in the design and simulation of one version of the novel bearing. Observations are given on the operation, success rates and verifications of the computational process. Copyright © 1999 John Wiley & Sons, Ltd.

KEY WORDS: finite difference; finite element; adjustable hydrodynamic bearing

1. INTRODUCTION

Hydrodynamic fluid film bearings are widely used in many areas of mechanical engineering, e.g. turbines, engines, pumps, gearboxes, etc., in aircraft, road and rail vehicles, ships, generating plant, machine tools and many other applications where rotating parts are supported. Generating their own oil film pressures, they can carry large loads, provide significant stiffness and damping, while preventing physical contact between the bearing surfaces. They can be of radially and axially supporting forms. The radial type most commonly comprises a shaft or journal rotating within a stationary bearing housing. Less common is the inverse arrangement of a rotor on a stationary journal. The axial form is the thrust bearing, where the rotating member bears on thrust faces reacting axial loads. The principles of hydrodynamic lubrication apply equally to all forms.

Hydrodynamic lubrication is a self-sustaining fluid film separation of the two bearing surfaces. Loads are carried by pressures generated independently of supply pressure, the latter merely ensuring adequate supply of lubricant. The lubricant, almost always oil, must have significant viscosity, there must also be considerable relative motion of the surfaces, and the oil

* Correspondence to: Engineering Mechanics Lubrication Research Group, The Open University, Milton Keynes, MK14 5AS, UK.

film shape must at some part be convergent. The phenomenon was put on a mathematical footing by Reynolds in 1886 and most hydrodynamic lubrication theory involves some form of Reynolds' pressure field equation. This equation relates velocity- and pressure-induced fluid flows based on the assumptions of continuity of volume flow rate and equilibrium of fluid film forces. It predicts that substantial pressures and pressure gradients are generated that oppose converging flows (and boost diverging flows). It is by such pressure fields that surface separation can be maintained ensuring full film lubrication under large loads.

Although the design of bearings in general is well-documented, the continuing desire for better performance in terms of higher speeds, lower energy losses, vibration suppression, accuracy of location, noise signatures, etc., has lead to increased attention focusing on bearing behaviour. In addition, some hitherto satisfactory bearings are failing drastically under increasingly severe performance demands.

A novel form of adjustable fluid film bearing has been devised whereby the hydrodynamic conditions can be changed in an externally and continuously controlled manner during operation. The principle can be applied to conventionally orientated journal bearings, to inverse orientations, and to thrust bearings. The embodiments are included in international patent applications filed by British Technology Group Ltd. [1]. Investigations have been carried out on theoretical and practical models for journal bearings of both orientations. The novel bearing has demonstrated significant improvements over conventional bearing designs in terms of stiffness, damping, rotational accuracy, power losses and temperature rise. Performance characteristics predicted by the computer model have been demonstrated in practice.

Herein is described the comprehensive mathematical model of the novel bearing and an automated computational process devised to produce solutions for a variety of simulated operating conditions. It was designed and developed to be applicable to all forms of the bearing and was used extensively to study, and optimise, the design of a particular type of the inverse arrangement comprising a rotor supported by a stationary journal. Figure 1 shows this

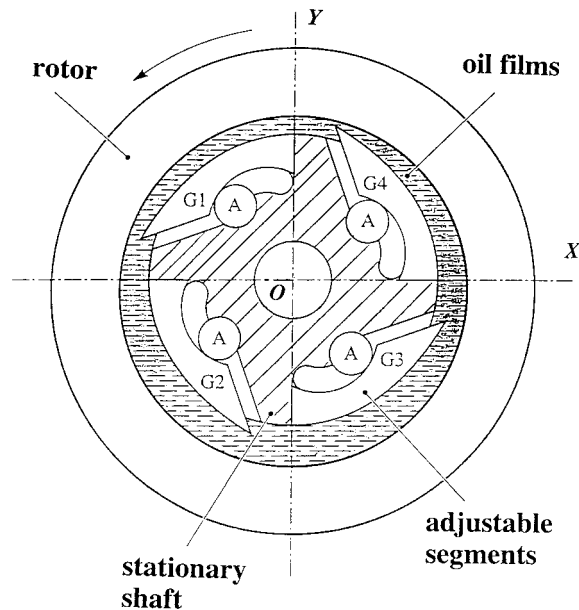


Figure 1. Adjustable hydrodynamic bearing concept.

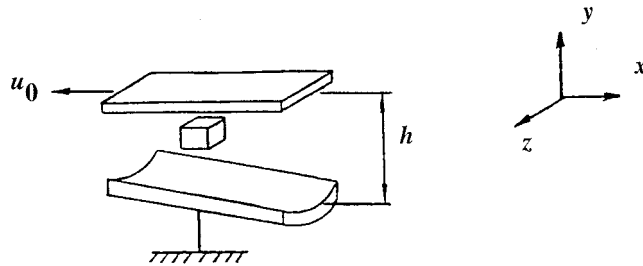


Figure 2. Hydrodynamic lubrication fluid element.

in outline form with displacements greatly exaggerated for clarity. There are four adjustable cantilevered segments, G1, G2, G3 and G4, each supported by adjuster pins labelled 'A'. The principle of the bearing was that the hydrodynamic conditions could be changed by independently controlled adjustments of the adjustable segment shapes and positions. This was effected by position change inputs to the adjuster pins, 'A'.

The mathematical model included an enhanced expansion of the governing Reynolds' equation, a finite difference approximation and a computerised Gauss–Seidel iterative solution technique. The adjustable segments of the bearing were simulated by finite element models that interacted automatically with the fluid film pressure field solutions as they arose. Thus, the 'elasto-hydrodynamic' effects of the fluid film shapes on pressure (and *vice versa*) were allowed for. In addition, a finite difference temperature field approximation was devised and viscosity allowed to vary with temperature and pressure.

The automated computing process involved an indexing cycle of successive finite element and finite difference computations. In general, full simultaneously converged field solutions for fluid film profile thickness, temperature, viscosity and pressure were regularly obtained for all but the severest of load conditions. By this means a great many predicted performance characteristics were studied. This paper outlines the design and development of the mathematical model and computation process itself and gives observations arising from its extensive use.

2. PRESSURE FIELD

The governing Reynolds' equation for the fluid film pressure field acting on one adjustable segment was derived with reference to the fluid element depicted in Figure 2. Pressure, film thickness and viscosity were set to vary in two dimensions; circumferentially around (x) and axially along (z) the segment surface. The derivation was based on a number of assumptions, most of which are normally invoked as follows:

- Fluid density constant (i.e. not affected by pressure or temperature).
- Fluid acceleration forces negligible compared with viscous shear forces.
- Weight of fluid is negligible.
- Film thickness small compared with radii of curvature.
- Pressure constant radially through film thickness at each point.
- Viscosity constant radially through film thickness at each point.
- Viscosity a variable independent of pressure (initially).
- Relative inclination of bearing surfaces is small, $\sin \theta \rightarrow \theta$, $\cos \theta \rightarrow 1$.
- No fluid slip at fluid bearing surfaces.

- No loss of fluid due to leakage.
- Constant volume flow rate.
- Fluid forces in equilibrium.
- Fluid is Newtonian.

For steady loading conditions, the Reynolds' equation as formulated was

$$\frac{\partial}{\partial x} \left(h^3 \eta^{-1} \frac{\partial P}{\partial x} \right) + \frac{\partial}{\partial z} \left(h^3 \eta^{-1} \frac{\partial P}{\partial z} \right) = 6u_0 \frac{\partial h}{\partial x}. \quad (1)$$

It is identical to the form usually quoted for conventional rotating journal bearings. Thus, with an appropriate choice of reference axes, the same Reynolds' equation was applicable for the case of a rotating bearing housing on a stationary journal.

It is customary to non-dimensionalise all the variables to simplify numerical analysis, and to make the computation algorithms more general. This was done with a view to treating analysis programs as aids to design.

The variables were non-dimensionalised as:

$$\bar{x} = \frac{x}{\pi D}, \quad \bar{z} = \frac{z}{B_L}, \quad H = \frac{h}{C_r}, \quad \bar{\eta} = \frac{\eta}{\eta_1}, \quad \bar{P} = \frac{P}{\omega \eta_1 (R/C_r)^2}.$$

The Reynolds' equation became

$$\frac{\partial}{\partial \bar{x}} \left(\frac{H^3}{\bar{\eta}} \frac{\partial \bar{P}}{\partial \bar{x}} \right) + \left(\frac{\pi D}{B_L} \right)^2 \frac{\partial}{\partial \bar{z}} \left(\frac{H^3}{\bar{\eta}} \frac{\partial \bar{P}}{\partial \bar{z}} \right) = 12\pi \frac{\partial H}{\partial \bar{x}}. \quad (2)$$

This is in dimensionless form with \bar{P} , H , $\bar{\eta}$ variables in x - and z -directions.

It is also standard practice to use a substitution parameter $\bar{P} = P^* H^{-3/2}$, first used by Vogelpohl [2]. The main advantage is in smoothing the pressure derivatives and improving the accuracy of numerical solutions. The value of the exponent, $-3/2$, had another advantage in eliminating one of the pressure derivative terms.

Using this substitution, Equation (2) became

$$\frac{\partial}{\partial \bar{x}} \left(\frac{H^3}{\bar{\eta}} \frac{\partial}{\partial \bar{x}} (P^* H^{-3/2}) \right) + \left(\frac{\pi D}{B_L} \right)^2 \frac{\partial}{\partial \bar{z}} \left(\frac{H^3}{\bar{\eta}} \frac{\partial}{\partial \bar{z}} (P^* H^{-3/2}) \right) = 12\pi \frac{\partial H}{\partial \bar{x}}. \quad (3)$$

To expand this equation for the conventional type of journal bearing analysis it is usual to assume that the surfaces are perfectly cylindrical and their axes in line, in which case both derivatives of H by \bar{z} are zero, i.e.

$$\frac{\partial^2 H}{\partial \bar{z}^2} = \frac{\partial H}{\partial \bar{z}} = 0.$$

Furthermore, derivatives of H by \bar{x} can usually be expressed by differentiation of an expression for H . In this work none of these could be assumed, and indeed it was an advantage not to, in order to provide the options to analyse various adjuster surface shapes. Thus, Equation (3) required full development of the differential products of P^* , H and $\bar{\eta}$.

For simplicity, letting $A = (\pi D/B_L)^2$, the expanded Reynolds' equation was derived as

$$\begin{aligned} & H^{3/2} \bar{\eta}^{-1} \frac{\partial^2 P^*}{\partial \bar{x}^2} - H^{3/2} \frac{\partial P^*}{\partial \bar{x}} \bar{\eta}^{-2} \frac{\partial \bar{\eta}}{\partial \bar{x}} + \bar{\eta}^{-1} \frac{\partial P^*}{\partial \bar{x}} \frac{3}{2} H^{1/2} \frac{\partial H}{\partial \bar{x}} - \frac{3}{2} P^* H^{1/2} \bar{\eta}^{-1} \frac{\partial^2 H}{\partial \bar{x}^2} \\ & + \frac{3}{2} P^* H^{1/2} \frac{\partial H}{\partial \bar{x}} \bar{\eta}^{-2} \frac{\partial \bar{\eta}}{\partial \bar{x}} - \frac{3}{4} \bar{\eta}^{-1} \left(\frac{\partial H}{\partial \bar{x}} \right)^2 P^* H^{-1/2} - \frac{3}{2} \bar{\eta}^{-1} \frac{\partial H}{\partial \bar{x}} H^{1/2} \frac{\partial P^*}{\partial \bar{x}} + A H^{3/2} \bar{\eta}^{-1} \frac{\partial^2 P^*}{\partial \bar{z}^2} \end{aligned}$$

$$\begin{aligned}
& -AH^{3/2} \frac{\partial P^*}{\partial \bar{z}} \bar{\eta}^{-2} \frac{\partial \bar{\eta}}{\partial \bar{z}} + A\bar{\eta}^{-1} \frac{\partial P^*}{\partial \bar{z}} \frac{3}{2} H^{1/2} \frac{\partial H}{\partial \bar{z}} - \frac{3}{2} AP^* H^{1/2} \bar{\eta}^{-1} \frac{\partial^2 H}{\partial \bar{z}^2} \\
& + \frac{3}{2} AP^* H^{1/2} \frac{\partial H}{\partial \bar{z}} \bar{\eta}^{-2} \frac{\partial \bar{\eta}}{\partial \bar{z}} - \frac{3}{4} A\bar{\eta}^{-1} \left(\frac{\partial H}{\partial \bar{z}} \right)^2 P^* H^{1/2} - \frac{3}{2} A\bar{\eta}^{-1} \frac{\partial H}{\partial \bar{z}} H^{1/2} \frac{\partial P^*}{\partial \bar{z}} = 12\pi \frac{\partial H}{\partial \bar{x}}. \quad (4)
\end{aligned}$$

The dynamic situation is usually modelled by considering the net translatory 'squeeze film' velocity in the radial direction at the position of the fluid element. To incorporate this velocity, a treatment by Cameron [3] was adopted and the effects of any misalignment of the journal and rotor axes, or any synclastic deformation of the adjuster segment surfaces were neglected (for this parameter only). This approach brought forth the two-dimensional Reynolds' equation, including the 'standard' squeeze film term as follows:

$$\frac{\partial}{\partial x} \left(h^3 \eta^{-1} \frac{\partial p}{\partial x} \right) + \frac{\partial}{\partial z} \left(h^3 \eta^{-1} \frac{\partial p}{\partial z} \right) = 6u_0 \frac{\partial h}{\partial x} + 12 \frac{\partial h}{\partial t}, \quad (5)$$

which is Equation (1) with the squeeze film term added.

Non-dimensionalising by letting $\bar{t} = t\omega$, and adding the squeeze film term, Equation (3) became

$$\frac{\partial}{\partial \bar{x}} \left(\frac{H^3}{\bar{\eta}} \frac{\partial \bar{p}}{\partial \bar{x}} \right) + \left(\frac{\pi D}{B_L} \right)^2 \frac{\partial}{\partial \bar{z}} \left(\frac{H^3}{\bar{\eta}} \frac{\partial \bar{p}}{\partial \bar{z}} \right) = 12\pi \frac{\partial H}{\partial \bar{x}} + 48\pi^2 \frac{\partial H}{\partial \bar{t}}. \quad (6)$$

The expanded Reynolds' equation (4) became similarly modified by the inclusion of the term $+48\pi^2(\partial H/\partial \bar{t})$ on the right-hand-side. Inertia effects of the lubricant itself were considered negligibly small for the range of velocity changes and eccentricities envisaged for the rotor. This was in accordance with findings of Yamada and Nakabayaski [4] and Nataraj *et al.* [5].

3. FINITE DIFFERENCE APPROXIMATIONS

Numerical solution techniques for hydrodynamic lubrication are well-reported. Jakeman [6] described a technique that allowed for modelling oil film cavitation, power loss and non-linear characteristics of displacement and velocity performance coefficients. Khadar [7] presented a numerical integral scheme that claimed advantages in programming and for bearings with irregular geometry. Knight and Barrett [8] assumed polynomial pressure distributions in the bearing axial direction and also demonstrated the improvements in modelling accuracy when viscosity was allowed to vary circumferentially.

Gero and Ettles [9] compared the merits of finite difference and finite element approximations for the Reynolds equation pressure field, albeit for steady iso-viscous flow. There was little to choose between them for lower-orders, although higher-order methods resulted in generally improved accuracy. The lower-order finite difference method allowed for simplicity of programming and boundary condition representation. They also suggested that elasto-hydrodynamic and thermodynamic effects could be viewed as solving a sequential series of simpler, uncoupled and steady problems. This was the approach used for the work discussed herein.

Finite difference approximations were made for derivatives of pressure, film thickness and viscosity for two dimensions x and z , and for temperature in the x -direction, which were then used to solve Equation (4) for one adjuster segment. A uniform mesh was assumed comprising 143 finite difference nodes distributed in the circumferential and axial directions by m and n respectively over the fluid film surface of one adjuster segment. The general node integer

location was i, j . It was found that in formulating the non-dimensional mesh spacing using parameters related to the full journal circumference, a reduction factor, σ , was necessary for the circumferential direction, for one segment length, where

$$\sigma = \frac{\text{circumferential length of adjuster surface}}{\text{total circumference of journal}}.$$

Figure 3 shows the developed surface of one journal adjuster surface. The oil supply was assumed to be of some linear distribution along $i = 1$.

The total mesh size was $m \times n$ nodes, starting at the origin 1, 1.

The distance between nodes in the circumferential (x or i) direction was $\sigma\pi D/(m-1)$, non-dimensionalised = $\sigma/(m-1)$.

The distance between nodes in the axial (z or j) direction was $B_L/(n-1)$, non-dimensionalised = $1/(n-1)$.

The finite difference approximations and simplification terms used were as follows:

$$\frac{\partial P^*}{\partial \bar{x}} = (P_{i+1,j}^* - P_{i-1,j}^*)B, \quad \frac{\partial P^*}{\partial \bar{z}} = (P_{i,j+1}^* - P_{i,j-1}^*)C,$$

$$\frac{\partial^2 P^*}{\partial \bar{x}^2} = (P_{i+1,j}^* + P_{i-1,j}^* - 2P_{i,j}^*)BB, \quad \frac{\partial^2 P^*}{\partial \bar{z}^2} = (P_{i,j+1}^* + P_{i,j-1}^* - 2P_{i,j}^*)CC,$$

$$\frac{\partial H}{\partial \bar{x}} = E_{i,j} = (H_{i+1,j} - H_{i-1,j})B, \quad \frac{\partial H}{\partial \bar{z}} = F_{i,j} = (H_{i,j+1} - H_{i,j-1})C,$$

$$\frac{\partial^2 H}{\partial \bar{x}^2} = EE_{i,j} = (H_{i+1,j} + H_{i-1,j} - 2H_{i,j})BB, \quad \frac{\partial H}{\partial t} = \frac{v_p}{C_r\omega},$$

$$\frac{\partial^2 H}{\partial \bar{z}^2} = FF_{i,j} = (H_{i,j+1} + H_{i,j-1} - 2H_{i,j})CC,$$

$$\frac{\partial \bar{\eta}}{\partial \bar{x}} = G_{i,j} = (\bar{\eta}_{i+1,j} - \bar{\eta}_{i-1,j})B, \quad \frac{\partial \bar{\eta}}{\partial \bar{z}} = O_{i,j} = (\bar{\eta}_{i,j+1} - \bar{\eta}_{i,j-1})C,$$

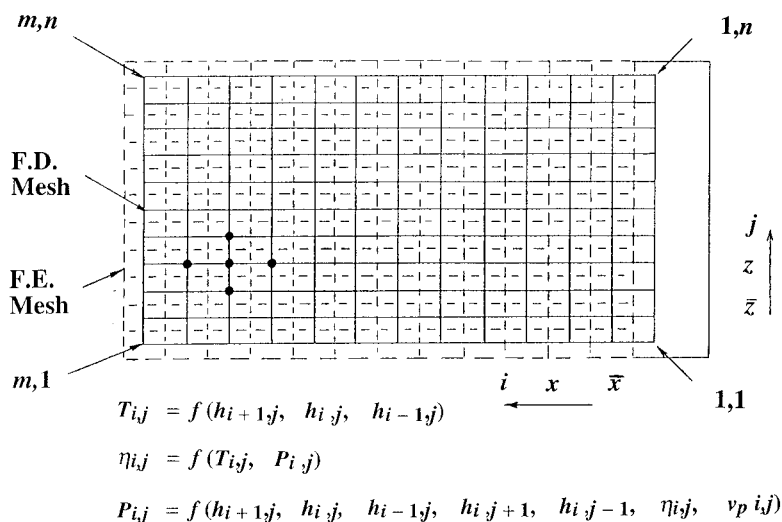


Figure 3. Finite difference and finite element meshes on adjustable segment bearing surface.

where

$$B = \frac{m-1}{2\sigma}, \quad C = \frac{n-1}{2}, \quad BB = \frac{(m-1)^2}{\sigma^2}, \quad CC = (n-1)^2;$$

letting

$$\begin{aligned} V_{i,j} &= \bar{\eta}_{i,j}, & R_{i,j} &= \frac{(H_{i,j})^{1.5}}{V_{i,j}}, & S_{i,j} &= -\frac{(H_{i,j})^{1.5}}{V_{i,j}^2} G_{i,j}, \\ ST_{i,j} &= \frac{1.5(H_{i,j})^{0.5}}{V_{i,j}} E_{i,j}, & U_{i,j} &= \frac{-1.5(H_{i,j})^{0.5}}{V_{i,j}} EE_{i,j}, \\ X_{i,j} &= -\frac{1.5(H_{i,j})^{0.5}}{V_{i,j}^2} E_{i,j} G_{i,j}, & Y_{i,j} &= \frac{-0.75(E_{i,j})^2}{V_{i,j}(H_{i,j})^{0.5}}, \\ Q_{i,j} &= \frac{-1.5E_{i,j}(H_{i,j})^{0.5}}{V_{i,j}}, & OO_{i,j} &= \frac{A(H_{i,j})^{1.5}}{V_{i,j}}, \\ PP_{i,j} &= \frac{-A(H_{i,j})^{1.5}}{V_{i,j}^2} O_{i,j}, & QQ_{i,j} &= \frac{1.5A(H_{i,j})^{0.5}F_{i,j}}{V_{i,j}}, \\ SS_{i,j} &= \frac{-1.5A(H_{i,j})^{0.5}FF_{i,j}}{V_{i,j}}, & TT_{i,j} &= \frac{-1.5A(H_{i,j})^{0.5}F_{i,j}O_{i,j}}{V_{i,j}^2}, \\ UU_{i,j} &= \frac{-0.75A(F_{i,j})^2}{V_{i,j}(H_{i,j})^{0.5}}, & VV_{i,j} &= \frac{-1.5A(H_{i,j})^{0.5}F_{i,j}}{V_{i,j}}, \\ WW_{i,j} &= 12.0\pi E_{i,j} + 48.0\pi^2 \frac{\partial H}{\partial t} \text{ (including squeeze film velocity term).} \end{aligned}$$

Substituting in the expanded Reynolds' equation with the variables H and $\bar{\eta}$ in finite difference form gave

$$\begin{aligned} \frac{\partial^2 P^*}{\partial \bar{x}^2} R_{i,j} + \frac{\partial P^*}{\partial \bar{x}} (S_{i,j} + ST_{i,j} + Q_{i,j}) + P^* (U_{i,j} + X_{i,j} + Y_{i,j} + SS_{i,j} TT_{i,j} + UU_{i,j}) \\ + \frac{\partial^2 P^*}{\partial \bar{z}^2} OO_{i,j} + \frac{\partial P^*}{\partial \bar{z}} (PP_{i,j} + QQ_{i,j} + VV_{i,j}) = WW_{i,j}. \end{aligned}$$

The finite difference forms for the pressure parameter terms were expanded and rearranged to give an equation for pressure parameter P^* . The following substitutions were used:

$$\begin{aligned} XX_{i,j} &= (S_{i,j} + ST_{i,j} + Q_{i,j}), & YY_{i,j} &= (PP_{i,j} + QQ_{i,j} + VV_{i,j}), \\ SSS_{i,j} &= (BB)R_{i,j} + (B)XX_{i,j}, & TTT_{i,j} &= (BB)R_{i,j} - (B)XX_{i,j}, \\ UUU_{i,j} &= (CC)OO_{i,j} + (CC)YY_{i,j}, & VVV_{i,j} &= (CC)OO_{i,j} - (C)YY_{i,j}, \\ RRR_{i,j} &= (U_{i,j} + X_{i,j} + Y_{i,j} + SS_{i,j} + TT_{i,j} + UU_{i,j} - 2(BB)R_{i,j} - 2(CC)OO_{i,j}). \end{aligned}$$

The pressure parameter equation became

$$P_{i,j}^* = \frac{WW_{i,j} - (SSS_{i,j})P_{i+1,j}^* - (TTT_{i,j})P_{i-1,j}^* - (UUU_{i,j})P_{i,j+1}^* - (VVV_{i,j})P_{i,j-1}^*}{RRR_{i,j}}. \quad (7)$$

This was now in a form ready for numerical computation, provided information about the viscosity profile field was also known.

4. TEMPERATURE AND VISCOSITY

A model for temperature prediction was formulated based on an assumed adiabatic model developed and simplified by McCallion *et al.* [10] further modified by Pinkus and Bupara [11]. In this, heat generated by oil film shear was assumed to raise the temperature of the oil itself only, and that this heat could only leave the bearing in the oil. This model was adapted to relate temperature of the fluid film to the finite difference approximation of its thickness profile, with temperature at a given node assumed constant through the thickness. The main results were

$$T = T_1 + \beta^{-1} \ln \left(e^{\psi_1} + AA \left[\frac{1}{H_{i-1}^2} + \frac{4}{H_i^2} + \frac{1}{H_{i+1}^2} \right] \right), \quad \text{where } AA = \frac{\sigma E}{3(m-1)}. \quad (8)$$

An oil viscosity–temperature exponential index equation was assumed of the form

$$\eta_T = \eta_1 e^{-\beta(T - T_1)}.$$

If the viscosity values at T_1 and T_{REF} were known, then β could be determined from

$$\beta = \frac{\ln \frac{\eta_{\text{REF}}}{\eta_1}}{T_1 - T_{\text{REF}}}.$$

Knowing the temperature field $T_{i,j}$, the viscosity field could be calculated using the viscosity–temperature equation quoted above, i.e.

$$\eta_{i,j} = \eta_1 e^{-\beta(T_{i,j} - T_1)}.$$

Oil chosen was a straight mineral oil to ISO VG 32 [12] after detailed computations with this and grades 22 and 46. Using available viscosity characteristic curves for such an oil, and in this instance taking account of temperature corrected densities, the following reference data were chosen for the viscosity model:

$$\begin{aligned} T_1 &= 40^\circ\text{C} & T_{\text{REF}} &= 85^\circ\text{C} \\ \eta_1 &= 0.0285 \text{ Pas} & \eta_{\text{REF}} &= 0.0064 \text{ Pas} \end{aligned}$$

Regarding possible effects of pressure on viscosity, other empirical data proposed by Cameron [3,13] were adopted. These predict that an increase of pressure increases viscosity. In extreme conditions this is a useful feature as the regions of high pressure were in or near regions of high temperature; thus, large reductions in viscosity due to temperature rise could be partially offset by some increase due to pressure rise. Although not forming part of the Reynolds' equation derivation, these data were incorporated in the main iteration loop to operate on pressure values as they arose. In general, predicted pressures were not high enough for the effect on viscosity to be greatly significant. Increases in computer processing time were negligibly small so the algorithm was left in. Largely for historical reasons the constants in this empirical model relate to UK units, and conversion to SI was left until the final stage of computation to avoid possible sources of error. If the value $\eta_{2(i,j)}$ was already updated from $\eta_{1(i,j)}$ to include temperature effects, the pressure affected viscosity $\eta_{3(i,j)}$ was then given by:

$$\eta_{3(i,j)} = \eta_{2(i,j)} (1.0 + \lambda P_{i,j})^{16},$$

where

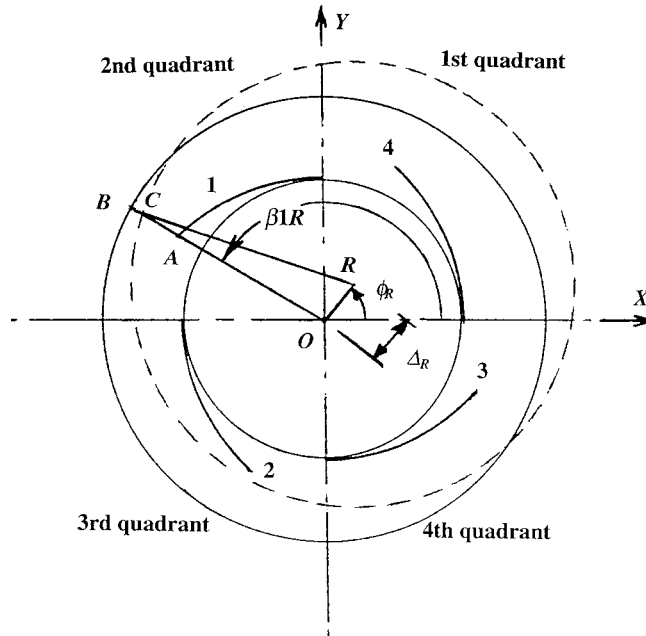


Figure 4. Rotor radial displacement.

$$\lambda = 10^a(0.062)\eta_{2(i,j)}^{-0.062} \quad \text{and} \quad a = -\left(0.4 + \frac{T_{i,j}(\text{°F})}{400}\right).$$

For both viscosity and pressure fields, information about the film thickness variation around and along the bearing was needed.

5. ROTOR TRANSLATORY DISPLACEMENT AND VELOCITY

General rotor displacement, in two dimensions, comprised both x and y components. The change of film thickness due to a general resultant displacement Δ_R at reference angle ϕ_R was determined for each of the four segment surfaces, with displacements being in all four polar quadrants, i.e. 16 separate analyses. This number was necessary because each segment could be independently and uniquely adjusted, and the rotor could adopt a position centred in any of four polar co-ordinate quadrants. Figure 4 shows the geometrical considerations of a rotor displacement Δ_R at an angle ϕ_R in the first polar quadrant, and the effect on the film thickness profile for segment G1 in its quadrant.

Displacements in other quadrants, repeated for the other three segments, were treated in a similar manner.

The segment fluid film profiles could be determined from the initial geometry of the system, the resulting displacements of the adjustable segment surfaces, and any displacements, i.e. eccentricity, of the axis of rotation of the rotor. It was found that one general equation was suitable for describing each segment film thickness profile for rotor displacements in all four polar quadrants. It was of the form

$$h(1-4)R_{i,j} = h(1-4)_{i,j} - R_{RO} + \frac{R_{RO}}{\sin(ROC(1-4)_{i,j})} \left(\sin\left(\pi - (ROC(1-4)_{i,j}) - \sin^{-1}\left(\frac{\Delta_R}{R_{RO}} \cdot \sin(ROC(1-4)_{i,j})\right)\right) \right)$$

For the dynamic situation the appropriate rotor translatory velocity could be set as an input vector. The rotor was considered to have a translatory velocity of v_R at known reference angle ψ , which could be resolved as appropriate into the relevant squeeze film velocities. Figure 5 shows a velocity vector in the first quadrant to be resolved for a point on segment G1 in its quadrant. For a small rotor displacement the translating rotor velocity components at angle $\beta 1R$ can be approximated to

$$v_p = v_R \cos(\pi - \beta 1R + \psi), \quad v_t = v_R \sin(\pi - \beta 1R + \psi).$$

So for each point

$$u_0 = \frac{\omega D}{2} - v_t \quad \text{and} \quad \frac{\partial h}{\partial t} = v_p.$$

For most practical conditions perceived in the application of the bearing system it was assumed that the translatory velocity of the rotor would be orders of magnitude smaller than the rotor tangential velocity due to its rotation. Thus, the rotor tangential velocity u_0 could be regarded as a constant for all points, being equal to $\omega D/2$. This was represented by the constant term u_0 in the Reynolds' equation. Inclusion of v_t would make u_0 a function of angular position and require a cumbersome treatment in the equation. Although this was possible in the computer programs the idea was not pursued.

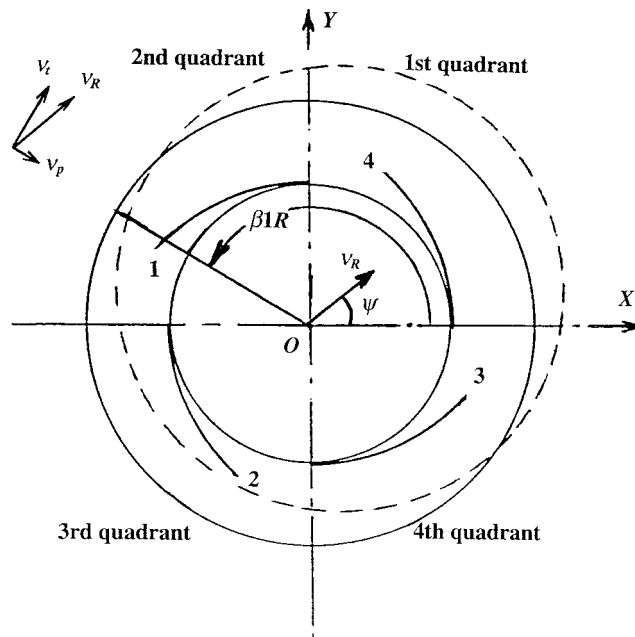
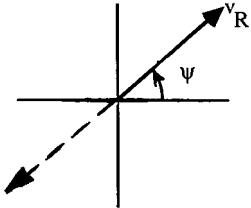
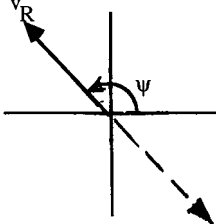


Figure 5. Rotor radial velocity.

Table I. Squeeze film velocity node equations

Squeeze film velocity	Rotor velocity polar quadrant
$V1RP(I, J) = v_R \cos(\beta 1R_{i,j} - \psi)$ $V2RP(I, J) = -v_R \cos(\psi + \pi - \beta 2R_{i,j})$ $V3RP(I, J) = -v_R \cos(\beta 3R_{i,j} - \pi - \psi)$ $V4RP(I, J) = v_R \cos(\psi - \beta 4R_{i,j})$	1st & 3rd 
$V1RP(I, J) = v_R \cos(\psi - \beta 1R_{i,j})$ $V2RP(I, J) = v_R \cos(\beta 2R_{i,j} - \psi)$ $V3RP(I, J) = -v_R \cos(\psi + \pi - \beta 3R_{i,j})$ $V4RP(I, J) = v_R \cos(\psi - \beta 4R_{i,j})$	2nd & 4th 

The implications for all four segments were considered, each with rotor displacements in all four quadrants, and rotor translatory velocities also in all four quadrants.

The rotor translatory velocity vector was considered in polar co-ordinates with conventional sign convention. Thus, for each segment profile the perpendicular squeeze film velocity at any point could be negative or positive depending on the angles concerned. Care was taken to check for 'closing or opening' squeeze film values at each point.

It was found that two sets of four equations were necessary to describe all segment squeeze film velocity profiles, for general rotor velocities in all four polar quadrants.

These are given in Table I. Quadrants 3 and 4 could be covered by reversing the sign of v_R in the appropriate set of equations.

6. FINITE ELEMENT MODEL

The adjuster segments were modelled using proprietary finite element software including a pre-processor and direct access to a solver. Linear statics analysis was used producing displacements in Cartesian co-ordinates for all element nodes, from which stresses were automatically computed using appropriate material data which in this case was steel to BS970 (1991) 655M13 (equivalent to En36) [14]. A range of checks and verifications were carried out using *in situ* routines, manual calculations, etc. Model files were created using mapped mesh generation, in preference to fully automatic generation, in order to retain control of element location and node numbering sequences.

A key feature was to arrange the finite element faces representing the adjustable segment surface in contact with the fluid film such that the face centroids coincided with finite difference node positions for the pressure field solution (Figure 3). By this means a field of pressures could be applied directly to the surface with each finite difference nodal pressure value being applied to the relevant finite element face. This effectively specified the size and orientation of the finite element mesh.

The chosen finite difference mesh comprised a pattern of 13×11 nodes. One hundred and thirty-two of these nodes were to be positioned at finite element face centroids. The oil film surface of the adjustable segment, thus needed 132 elements. A mapped distribution of elements throughout the model to produce this face resulted in a finite element solid model comprising 528 elements.

To check accuracy, a model was repeatedly analysed using a range of element mesh specifications for the same applied loading conditions. Stresses were computed for increasingly fine element specifications and the iteration effect of results noted. For each specification the nodes at the fixed end of the segment were restrained to have zero degrees of freedom, and the nodes nearest a notional position of the adjuster pin had a load set applied. This adjuster force was divided into a number of equal values, the number corresponding to the number of nodes, with the end node values being reduced by 50%. It was thus applied as an approximated distributed load of discrete values. Each node value was applied in Cartesian components (the axial component being zero) all making up a load set. This load set was optimised by repeated solutions to generate a computed displacement at the free end of the segment of 75% of the available concentric clearance, C_r .

In subsequent studies, particularly with pressure fields applied, the adjuster input was modelled as an imposed displacement restraint. The nodes representing the adjuster pin were specified with imposed displacements UX , UY equivalent to those produced with the input force case. Comparison of resulting data for both cases verified this alternative method. By using the imposed displacement the same adjuster input setting could be used for a variety of pressure load cases and the force reaction on the adjuster pin then computed from results data. Intermediate settings were specified by simple proportion.

The boundary condition in the region of the adjuster pin was in reality a complicated contact/rolling combination that could not easily be modelled. Predicted stress values in the pin region were therefore not reliable. They were, however, judged to be a worst case owing to the St. Venant effect that would occur in the real situation. By the same effect, results for elsewhere in the model would still be valid.

Segment models were constructed using parabolic and linear finite element types and compared one with another. In general, it was found that the linear element type was satisfactory for most conditions studied. This is discussed further below.

7. ITERATIVE COMPUTATION PROCESS

Holmes and Ettles [15] made a detailed study of iterative solution techniques compared with direct methods and concluded that iterative methods were easier to program and consumed less storage space. They also cautioned that neither method if applied to successive iterative solutions of coupled systems could be guaranteed to produce values that converged exponentially.

The computing process adopted for the work described herein applied to each segment and involved a repeated cycle shown in outline in Figure 6. It could be invoked any number of times (within limits) to take account of the elasto-hydrodynamic effect, and in most cases so tried did produce resulting pressure fields and fluid film profiles that simultaneously converged asymptotically towards a single solution, i.e. a given pressure field and film profile for each set of operating conditions. The process could then be indexed on to the next adjustable segment and repeated until solutions had been achieved for all segments.

Figure 7 shows this overall process in outline form. Only one finite element model file was necessary as all four segments were identical. Each of the four segments existed in a dedicated

subdirectory from which the model file could be addressed as appropriate. A suite of programs was written in Fortran 77 to carry out the numerical processing at key stages. All programs were verified and checked with specimen manual calculations. A range of specially written program files controlled and ran the computing process entirely automatically once initial conditions had been set. All programs were written in general terms to avoid the need to edit when changing system parameters, which were entered as data. The main steps in the process can be summarised as follows.

The operating conditions were entered in data files. These included individual segment adjustments, rotor position, rotor angular and translatory velocities. The process was then initiated and left to run automatically.

The first adjustable segment No. 1 was referenced and a finite element solution obtained for the given input conditions.

The finite element results data file was then interrogated by a specially written program. This scanned the data searching out relevant information for the nodes on the bearing segment surface. It extracted the initial x and y co-ordinates and final displacements UX and UY . The nodes targeted were mid-side finite element nodes adjacent to the element face centroid in the case of parabolic elements, or the corner nodes for linear elements. A dummy set of nodes corresponding to line $1, j$ was created by reflecting the line for $2, j$ initial positions with zero

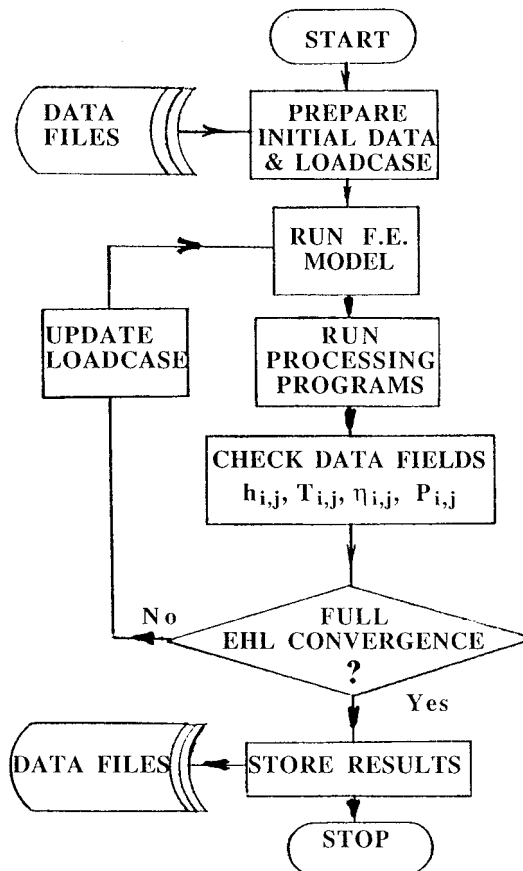


Figure 6. Overall computing process for 1 adjustable segment.

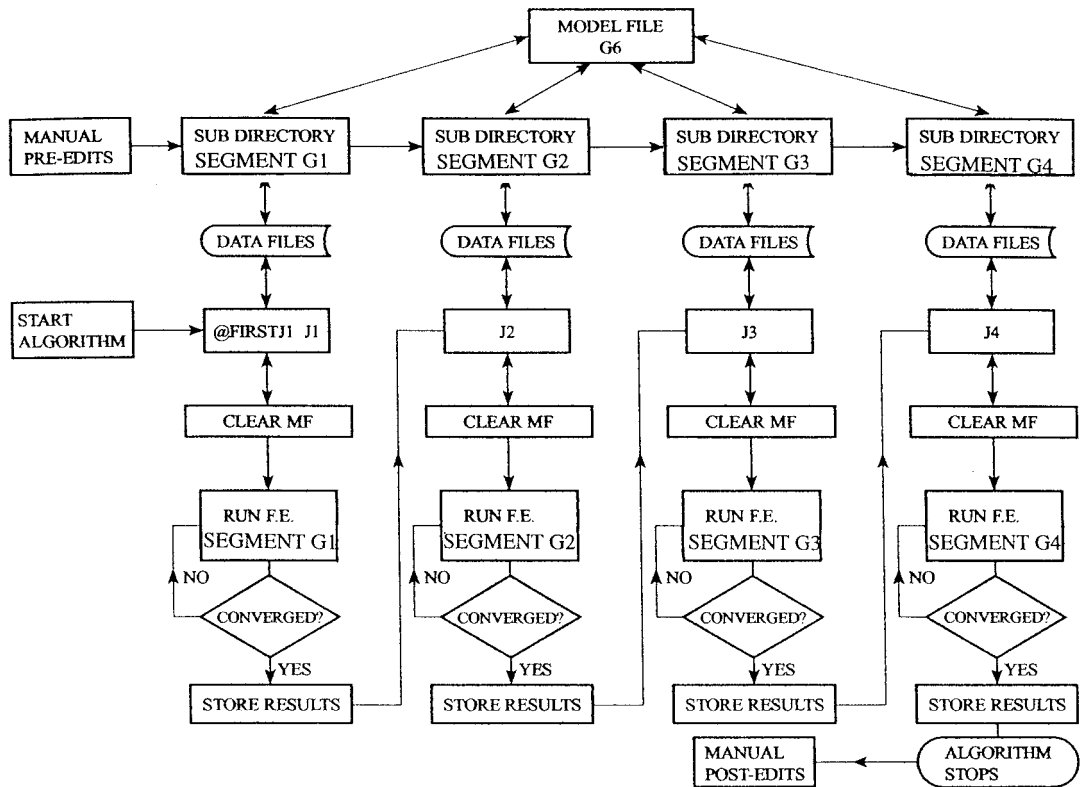


Figure 7. Overall computing process for whole bearing.

displacements. For each finite element node, the radial lubricant film thickness was calculated allowing for any rotor displacement and stored.

Each pair or corner groups' finite element film thickness values were then averaged to create a linear mid-position film thickness value at the element face centroid. This represented the required value for the finite difference node position. The nodal information representing the adjuster pin interface was also extracted, stored and processed to give an average pin node displacement or total reaction force as appropriate. Also computed were squeeze film velocity field profiles in the event of any input rotor translatory velocity representing the dynamic case.

The temperature and viscosity fields were then calculated and stored. A Gauss-Seidel iteration process was then invoked to produce the lubricant hydrodynamic field of pressures, beginning with an initial pressure field set at some low notional value with an assumed supply pressure distribution along $i = 1$. The edge pressures for $j = 1$, $j = n$ and $i = m$ were set at a negligibly small value to represent outlet atmospheric pressure (neglecting any vacuum assistance that may be needed for exhaust oil). It was known from previous work that various commonly assumed boundary conditions had little influence on solutions, so no other boundary conditions were specified. Negative value suppression was employed to set any calculated negative values of pressure parameter $P_{i,j}^*$ to zero as they arose to reflect more realistically the likely behaviour of the oil film.

This negated possible tensile viscosity properties of the oil. Another effect was to nearly double the number of pressure program iterations required for a full solution. Exhaust oil was assumed to be dispersed, without reforming as a lubricant film for the next adjustable segment.

Also input after the first cycle was a field of pressures solved for the previous overall cycle. Beginning the Gauss–Seidel iterative solution process, a converged pressure field was obtained based on the input viscosity field. This was defined as a converged solution when:

$$\text{for the } K\text{th iteration } |P_{i,j}^K - P_{i,j}^{K-1}| < PC |P_{i,j}^K|$$

for all values of i, j . The total number of iterations required was recorded and was usually less than 50, even for a PC value of 1%. The acceptance factor PC was usually set between 1 and 5%, for all values of i, j . This was influenced by the limits of expected accuracy of finite element models in general, and computing resources in particular.

The converged pressure field was then used to update the original viscosity field by invoking the pressure–viscosity relationship. A new convergent pressure field was then obtained, and the whole process repeated until the viscosity had converged to a solution defined by:

$$\text{for the } J\text{th iteration } |\eta_{i,j}^J - \eta_{i,j}^{J-1}| < PC |\eta_{i,j}^J|$$

for all values of i, j . Thus, both viscosity and pressure fields had converged to a solution. The number of converged nodes was recorded for each loop and usually increased rapidly giving a complete converged viscosity and pressure solution in only a few iterations, usually less than 10. In case a divergent solution occurred in any of the iteration loops, a limit value of iterations triggered a stop to the process and issued an appropriate message.

The successfully converged final pressure field was the solution for the latest input field of film thickness values. It was then compared with the solved pressure field obtained for the previous cycle field of film thickness values and the differences in nodal values noted. A solution was accepted when:

$$\text{for the } G\text{th iteration } |P_{i,j}^G - P_{i,j}^{G-1}| < PC |P_{i,j}^G|.$$

This check was a measure of convergence to a final lubricant film shape profile. The film thickness profile field values themselves were not used for cycle comparisons owing to the likely smallness of changes in values and consequent ill-conditioning errors. Provision was made for successive over relaxation.

If the film thickness profile field had not yet converged, a universal file of the finite difference node pressures was used to automatically create a new pressure load case set for the finite element analysis program. This new load set of pressures was applied to the adjuster segment model and a fresh finite element solution obtained. This gave a new field of finite element nodal displacements. The whole process was repeated cyclically until the pressure field had converged to a solution within limits of that of the previous film thickness profile, as set by PC above. By this means the elasto-hydrodynamic effect of the pressure field on the adjustable segment was included.

Once the given segment had been successfully analysed with resulting mutually satisfied convergent fields of film thickness, temperature, viscosity and pressure obtained, these and other data, such as iteration records, etc., were stored. The process then indexed on automatically to the next adjustable segment and the whole process was repeated. After all four adjustable segments had been thus analysed, the automated process halted and various post-processing operations were carried out.

One important parameter was the resultant oil film force. Each segment finite element bearing surface was associated with a pressure value and for an element of face area EA and at angle θ from a given reference axis an oil film force could be computed for the complete segment as follows:

$$F_x = \sum f_x = \sum_{i=1}^{i=m} \sum_{j=1}^{j=n} P_{i,j}(EA) \sin \theta,$$

$$F_y = \sum f_y = \sum_{i=1}^{i=m} \sum_{j=1}^{j=n} P_{i,j}(EA) \cos \theta.$$

The net force for all four segments could be simply determined by vectorial resolution. These operations were included in the pressure and post-processing programs.

8. DISCUSSION AND RESULTS

It is hoped that the full range of theoretical studies and predicted performance of the bearing itself will be reported separately, along with practical testing carried out on a real version of the bearing. Details of both are reported by Martin [17]. The main findings of using the computation method are discussed below.

The computation process was carried out using a suite of centrally supported minicomputers and took a minimum of about 3 h CPU time to achieve a full EHL solution for one set of conditions, for all four segments. Batch processing was therefore used with elapsed times that varied from about 4 h at best to over 3 days at worst for a single run. Access via modem was straightforward and permitted monitoring 'round the clock' and initiation of new runs as convenient avoiding peak use times. A total of 483 runs was successfully completed to produce the results reported representing about 1500 h CPU time. Success rate of solution starts was well over 90%.

The process was occasionally vulnerable to changes in the proprietary F.E. Software. Experience showed that version updates tended to include unannounced changes in either control commands or output formats. A typical example was an unheralded change in menu name for load set from L to S. This meant that program files had to be edited wherever a load set call had been incorporated.

Another area needing some care was treatment of data files following a system crash. It was important not to use interactive-type purge commands in program files in case relevant current data files were inadvertently deleted as the process tried to continue after stopping. It was also possible in these circumstances for large temporary scratch files to be left residing on a dedicated disk that could not be conveniently deleted without privileged access.

Generally, the overall process was robust and reliable, susceptible only to disk space limits being exceeded. It was noted that the model file itself tended to grow in size, thereby consuming disk space. This was because the database perpetually increased with the number of load set changes and deletes. Delete and save commands did not purge the model file itself. The only way to do this was to recreate it, either directly or indirectly using universal file transfer. Direct recreation inevitably brought problems with interim version changes that may have occurred. The problem was efficiently by-passed, however, by storing a clean copy of the model file and copying it up to overwrite the working model file, whenever necessary.

The analysis process was used initially to design the shape of the adjustable segment including the position of the adjuster pin. After such detailed studies, the pin was positioned on the underside nearer (but not directly) opposite the region of computed centre of pressure to minimise bending effects. This also gave advantages in terms of packaging and stiffness of the main shaft.

It was established that the film shape resulting from the adjuster only mode (i.e. the first overall iteration) produced peak pressures and total pressure forces invariably higher than

subsequently generated shapes allowing for the elasto-hydrodynamic effect. Results also showed that the first iterated shape produced the worst case loads for stressing purposes. The effect of the induced first loop pressure forces was to increase the reaction force at the adjuster pin by a factor of eight or nine times, and local stress values by about five times over the displaced segment only case with no pressures. It was also noted that the effect of scalloping the underside of the design was that under the influence of pressure loads the stresses were spread approximately uniformly throughout the segment length, an efficient use of material.

Comparisons with the adjuster input only mode with no pressures, showed that the elasto-hydrodynamic pressure field increased stresses for all models by about 30%. The adjuster pin reaction however increased by a factor of between 2.5 and 5 depending on the degree of scalloping.

It was noted that the peak pressures dropped when allowance was made for elasto-hydrodynamic effects, and the location of the peak pressure advanced slightly for all models ($P_{9,6}$ to $P_{8,6}$).

The use of linear elements instead of parabolic elements was investigated. Data in these models were identical to those in the parabolic element models with the exception of the element specification (i.e. linear instead of parabolic). The finite elements were thus interconnected only at corner nodes with no mid-side node connections. Minimum modifications were necessary for the processing software, it having been written to be as general as possible. The main changes were in node numbering references and the processing of the element centroid finite difference film thickness from four corner nodes instead of the mid side nodes. Cases studied were again for an adjustment pin setting giving 75% 'consumed' radial clearance with zero rotor eccentricity, in both rigid and EHL modes.

In rigid mode computed data were very close for both linear and parabolic element models. The stress plots for all the stresses (σ_{MAX} , σ_{MIN} , σ_{MS} , σ_{VM}) were correspondingly similar for the linear and parabolic cases, but the plots for the linear element model were less smooth and, significantly, indicated less clearly the small regions of highest stress.

In EHL mode the parabolic element model needed 14 iterations of finite element model solutions to converge to an overall solution based on a convergence factor of 1%. The linear element model took 16 runs to converge to a solution based on a convergence factor of 5%. Computed data for the two element types are shown in Table II.

It was noted that some corresponding data were significantly different and that the linear element model appeared to consistently predict a 'better' performance (e.g. lower temperature rise, higher pressures, larger oil film force, lower stresses etc.). Although depicting the same adjustment settings and load cases it was clear that the results were influenced by the type of finite element type specified, for the same sizes and numbers of finite elements. Care was therefore needed in interpreting results, particularly for the maximum adjustment cases.

As was expected with linear elements the computation for each finite element solution was speeded up considerably (e.g. approx. 5 minutes of CPU time instead of about 40). The resulting data files of node and element information and results were also smaller (e.g. 285 blocks compared to 970 approx.), which speeded up the results processing. In EHL mode, however, more finite element solutions were required to achieve an acceptable result, despite a more generous convergence factor. The advantage of much quicker finite element computations was therefore offset by the need to have more of them.

In addition, as has been seen there were some significant differences in calculated data resulting from the differences in film shape profiles derived from the finite element results. Since these data were highly influenced by small perturbations in the $h_{i,j}$ field, (as are all hydrodynamic lubrication conditions), the use of linear elements in the finite element models

was not pursued further for cases of large adjustment or high rotor eccentricities (i.e. situations producing very high pressures), and investigations for these conditions continued with the parabolic type. It was also shown that for eccentricity ratios greater than about 0.6 both linear element and parabolic element models of the most heavily loaded segment would only converge very slowly in EHL mode. Experiments were tried with successive overrelaxation that generally greatly accelerated convergence for these regimes, but some solutions diverged equally rapidly on continuance. Holmes and Ettles [15] cautioned that no methods of accelerating convergence of iterative solutions is universally applicable, including optimising methods for dynamically calculating successive over relaxation factors, such as presented by Brazier [16]. Such solutions were therefore not accepted, and no solutions achieved with overrelaxation were used in the parametric study.

It was noted that pressures and load capacities predicted for eccentricities of the order 0.6 were equivalent to those of a conventional bearing operating with eccentricities around 0.9. No attempts were made, therefore, to study in depth such extreme operating conditions, as one of the aims of the novel bearing design was to reduce eccentricities.

This aim was clearly met and the problem of accelerating convergences for extreme conditions thus receded in relevance.

Further studies were carried out for a range of rotor displacement angles, a small rotor displacement eccentricity value, and a small adjuster segment setting. Under these conditions rapid EHL convergences (i.e. 3 or 4 cycles to solution) were produced for each segment for both parabolic and linear finite element models.

Segments 1–4 inclusive were all set equally to an adjustment, h_A , of approximately 13.1×10^{-6} m. This was sufficient to produce oil film pressures and forces of significant values for each segment (but all balanced to zero when the rotor was concentric). A rotor eccentric displacement of 2.5×10^{-6} m was set for a range of rotor displacement angles 269.99°, 250°, 230° and 210°. Results are shown in Table III.

Table II. Data for EHL G6 linear and G4 parabolic elements, zero rotor eccentricity

Data	G6L (linear elements)	G4P (parabolic elements)
$h_{11,6}$ (mm)	0.0188	0.0177
$h_{12,6}$	0.0179	0.0167
$h_{13,6}$	0.0149	0.0128
$T_{11,6}$ (°C)	56.4	59.5
$T_{12,6}$	61.1	65.4
$T_{13,6}$	65.8	71.2
$P_{7,6}$ (MPa)	9.17	8.40
$P_{8,6}$	11.07	8.75
$P_{9,6}$	12.27	8.36
$P_{10,6}$	11.19	6.93
PF_{RES} (N)	4229.8	3669.0
@ θ_x (°)	40.00	55.0
R_{RES} (N)	5186.4	4147.0
@ θ_x (°)	57.2	37.4
σ_{MS} (MPa)	39.4	55.1
σ_{VM}	74.6	99.9

Table III. Effect of rotor displacement angle on full EHL solutions

ϕ_R (°)	269.99		250		230		210		
Segment	F_x (N)	F_y (N)	F_x (N)	F_y (N)	F_x (N)	F_y (N)	F_x (N)	F_y (N)	
1	P	-696.1	1015.4	-620.1	901.3	-559.5	807.5	-519.6	742.2
	L	-694.6	1022.2	-616.1	905.8	-556.9	813.5	-518.7	749.7
2	P	-705.1	-502.6	-721.9	-523.1	-749.8	-543.9	-809.6	-591.4
	L	-713.2	-503.1	-728.3	-522.6	-755.2	-543.1	-813.1	-589.6
3	P	682.2	-928.3	752.2	-1024.5	817.4	-1117.6	876.2	-1205.1
	L	679.2	-929.7	748.6	-1025.1	812.7	-1116.9	870.2	-1203.0
4	P	1290.0	924.6	1291.9	910.4	1251.2	876.2	1176.7	816.7
	L	1287.4	917.6	1289.1	902.8	1250.9	869.8	1176.7	810.2
Total		571.0	509.1	702.1	264.1	759.3	22.2	723.7	-237.6
		558.8	507.0	693.3	260.9	751.5	23.3	715.1	-232.7
F_R	P	765.0	41.7°	750.1	20.6°	759.6	1.7°	761.7	18.2°
	L	754.5	42.2	740.7	20.6	751.9	1.8	752.0	18.0

$\Delta_R = 0.0000025$ m; $RS = 2$ ($= 0.5 \times 0.75 \times C_R$); P, parabolic elements; L, linear elements.

It can be seen that for the conditions specified, full EHL solutions with parabolic elements and linear elements were within 6% of one another, and most within 1.5%. Thus linear elements could be used with advantage for lower values of effective eccentricity (i.e. < 0.6 approximately). Also noticeable was the symmetry predicted with loads and attitude angles being similar for any rotor displacement angle. The bearing system, therefore, appeared not to be sensitive to direction of loading and so could provide similar bearing forces in all directions for a given rotor displacement, with equal adjuster settings.

A comprehensive parametric study was carried out for both static and dynamic conditions, for both zero and non-zero operating eccentricities. This is reported fully by Martin [17] and it is hoped that further results will be published separately.

9. CONCLUSIONS

A comprehensive mathematical model has been developed for a novel adjustable hydrodynamic bearing taking account of non-linear variation in the lubrication field shape profile. Related temperature and viscosity models were also developed.

The governing Reynolds' pressure field equation was expanded to take account of the non-linear variations in viscosity and shape profile.

Finite difference approximations were used to prepare a pressure parameter equation in a form suitable for numerical computation, and for the temperature model.

The finite difference model was designed to interact automatically with a finite element model of the bearing adjustable segments. The finite element model itself was based on a proprietary pre-processor and solver with specially written control and processing programs to permit results interrogation, processing and continued sequential overall processing in an iterative manner. By these means, the elasto-hydrodynamic effect of the lubricant film shape on pressure and *vice versa* were allowed for.

Relative radial displacements and velocities between the bearing surfaces could also be incorporated leading to consideration of bearing stiffness and damping.

The mathematical model and computation process were designed to be applicable to various forms of adjustable hydrodynamic bearing, of any required dimensions, and were used extensively in designing and studying one particular version comprising a rotor supported on a stationary shaft.

The process produced convergent solutions for most conditions studied with success rates of over 90% of solution starts. Failures were due mainly to external problems (e.g. disk space, power failures, etc.) and occasionally to excessively severe input operating parameters delaying overall convergence.

It was noted that for normal range operating conditions, linear finite element models could be used with advantage in terms of processing time, but parabolic element models were necessary for more severe cases. Accelerated convergence techniques were not found reliable in producing truly converged solutions.

REFERENCES

1. J.K. Martin and D.W. Parkins, 'Fluid film bearings', *International (PCT) Patent Application WO-95/29346*, November 1995.
2. G. Vogelpohl, 'Beiträge zur Kenntnis der Gleitlager-ver.dt. reibung', *Forsch Hft. Ing. No. 386*, 1937.
3. A. Cameron, *Principles of Lubrication*, Longmans, London, 1966.
4. Y. Yamada and K. Nakabayashi, 'On the flow between eccentric rotating cylinders when the outer cylinder rotates', *Bull JSME*, **11**, 455–462 (1968).
5. C. Nataraj, H. Ashrafinon and N.K. Arakere, 'Effect of fluid inertia on journal bearing parameters', *STLE Trib. Trans.*, **37**, 784–792 (1994).
6. R.W. Jakeman, 'A numerical analysis method based on flow continuity for hydrodynamic journal bearings', *Tribol. Int.*, **17**, 325–333 (1984).
7. M.S. Khader, 'A generalised integral numerical solution metho for lubrication problems', *Trans ASME J. Tribol.*, **107**, 92–96 (1985).
8. J.D. Knight and L.E. Bartett, 'An approximate solution technique for multiple journal bearings including thermal effects, with comparison to experiment', *Trans ASLE*, **26**, 501–508 (1983).
9. L.R. Gero and C.M.McC. Ettles, 'An evaluation of finite difference and finite element methods for the solution of the Reynolds equation', *Trans ASLE*, **29**, 166–172 (1986).
10. H. McCallion, F. Yousif and T. Lloyd, 'The analysis of thermal effects in a full journal bearing', *Trans ASME J. Lub. Technol.*, **92**, 578–587 (1970).
11. O. Pinkus and S.S. Bupara, 'Adiabatic solutions for finite journal bearings', *Trans ASME J. Lub. Technol.*, **101**, 492–496 (1979).
12. ISO 3448 International Standard. *Industrial Liquid Lubricants-ISO-Viscosity Classification*, 1975 (E).
13. A. Cameron, *Basic Lubrication Theory*, Ellis Horwood, Chichester, 1983.
14. BS 970 British Standard. *Wrought Steels for Mechanical and Allied Engineering Purposes-Part 1*, 1996.
15. A.G. Holmes and C.M.McC. Ettles, 'A study of iterative solution techniques for elliptic partial differential equations with particular reference to the Reynolds equation', *Comput. Methods Appl. Mech. Eng.*, **5**, 309–328 (1975).
16. P.H. Brazier, 'An optimum SOR procedure for the solution of elliptic partial differential equations with any domain or coefficient set', *Comput. Methods Appl. Mech. Eng.*, **3**, 335–347 (1974).
17. J.K. Martin, 'Investigations into an adjustable fluid film bearing', *Ph.D. Thesis*, Cranfield University, March 1997.